Time-Variant Modal Parameters and Response Behavior of a Base-Isolated Building Tested on a Shake Table

Rodrigo Astroza,[a] Gonzalo Gutiérrez,[a] Christian Repenning,[a] and Francisco Hernández[b]

This paper presents the identification of the instantaneous modal properties and the experimental response of a full-scale, five-story base-isolated RC building tested on a shake table. A suite of earthquake motions of various intensities was applied to the building to progressively increase the seismic demand. The deterministic-stochastic subspace identification method is employed to estimate the variations of the modal properties of the building by employing a short-time windowing approach. The changes of the modal parameters during the seismic motions are tracked and analyzed. Observed and measured responses of the structure are analyzed and correlated with the variation of the identified modal parameters. The nonlinear behavior of the isolators generates the variation of the identified natural frequencies and equivalent damping ratios of the building, which change in agreement with the input motion intensity. A high correlation between the effective stiffness of the isolators and the instantaneous frequency of the first mode is found. The effective damping ratio of the isolation system and the instantaneous damping ratio of the fundamental mode of the building are highly correlated. [DOI: 10.1193/032817EQS054M]

INTRODUCTION

Seismic isolation is one of the technologies to protect civil structures and their nonstructural components and systems (NCSs) during earthquakes (Housner et al. 1997). In fact, the exceptional performance of isolated structures during strong ground motions has been empirically proved during several earthquakes worldwide (e.g., Celebi 1996, Kasai et al. 2013). For this reason, seismic isolation is widely used in earthquake-prone areas in the world. In the case of buildings, base isolation is the most common solution, resulting in an elongation of the fundamental period of the building and an increase of the energy dissipation capabilities of the system.

Analysis of the actual response of base-isolated (BI) buildings under strong earthquakes is still scarce because there are not many isolated structures that have been instrumented during strong ground motions. Celebi (1996), Stewart et al. (1999), and Nagarajaiah and Sun (2000) analyzed the response of instrumented BI buildings during the 1994 Northridge earthquake, while Furukawa et al. (2005) estimated the modal parameters of a BI building

[a] Universidad de los Andes, Facultad de Ingeniería y Ciencias Aplicadas, Monseñor Álvaro del Portillo N°12.455, Las Condes, Santiago, Chile
[b] Universidad de Chile, Departamento de Ingeniería Civil, Av. Blanco Encalada 2002, Santiago, Chile

instrumented during the 1995 Kobe earthquake. Siringoringo and Fujino (2014) analyzed the response and conducted the identification of the modal properties of a BI building instrumented during several seismic events in Japan, including the 2011 Tohoku earthquake.

Large-scale shake tables (e.g., Ogawa et al. 2001, Van Den Einde et al. 2004) have provided very valuable data and information to the earthquake engineering community, complementing data collected during real earthquakes. A series of shake table tests were conducted at the E-Defense shake table in Japan to study the response of buildings that were isolated with different technologies (Sato et al. 2011, Furukawa et al. 2013). In 2012, a fully furnished full-scale five-story reinforced concrete (RC) building, named BNCS building hereafter, was tested both isolated and fixed at its base on the UC San Diego shake table (Chen et al. 2016, Pantoli et al. 2016a, 2016b).

In this paper, global and local responses of the BI-BNCS building obtained during seismic tests are analyzed and discussed. In addition, the instantaneous modal properties of the BI-BNCS building are identified by using the deterministic-stochastic subspace identification method (DSI) applied to a moving short-time window of input-output acceleration data (Tobita et al. 1988, Moaveni and Asgarieh 2012, Loh et al. 2013) recorded during the seismic tests. Based on these results, the responses of the isolation system and the building are correlated with the variation of the identified modal properties.

DESCRIPTION OF TEST STRUCTURE

The test specimen was a full-scale, five-story RC structure equipped with a wide range of NCSs (Figure 1a). The building had one bay in the transverse direction and two bays in the longitudinal direction, which coincided with the direction of shaking (east-west). The plan dimensions of the building were 11.0 m and 6.6 m in longitudinal and transverse directions

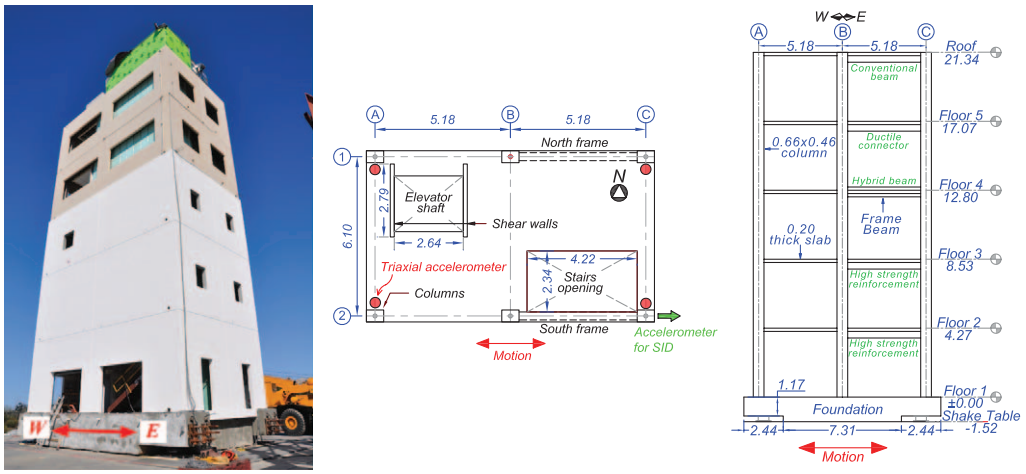

(a) (b) (c)

Figure 1. Test structure: (a) General view of the building; (b) plan view; (c) elevation view. (Dimensions in meters.)

(Figure 1b), respectively, and the story height was 4.27 m, reaching a total height, measured from the top of the foundation to the top of the roof slab, of 21.34 m (Figure 1c). The total weight of the building, excluding the foundation, was approximately 4,420 kN, with a contribution of about 75% (3,010 kN) from the bare structure and 25% (1,010 kN) from the NCSs, and the weight of the foundation was 1870 kN. A pair of one-bay special moment resisting frames, one on the north face and another on the south face of the building (Figure 1b), provided the lateral load resisting system in the longitudinal direction of the test specimen. The floor system consisted of a 0.20 m thick RC slab at each level. Six columns with cross-section dimensions of 0.66×0.46 m were reinforced with six #6 and four #9 longitudinal reinforcing bars and a prefabricated transverse reinforcement grid. Beams were built with a cross-section of 0.30×0.71 m and different design solutions were adopted at different floors (Figure 1c). Two RC shear walls with a thickness of 0.15 m were placed along the transverse direction of the building to add torsional stiffness and to accommodate the supporting system of the elevator. Detailed information about the test specimen and its design is described by Chen et al. (2016) and Pantoli et al. (2016a).

In a first testing phase, the building was mounted on four high-damping rubber bearings (HDRBs), which were located between the shake table platen and the foundation of the building close to the four corners of the building. The isolators had a total height of 0.34 m, comprised of 34 layers of rubber with a thickness of 6 mm each, 33 steel shim plates with a thickness of 3 mm each, and top and bottom steel plates with a thickness of 20 mm each (Figure 2a,b). The isolators had a rubber diameter of 0.65 m and a core diameter of 0.10 m (Figure 2a).

Prior to the shake table tests, each HDRB was individually tested under seven pseudo-static sinusoidal fully-reversed cycles reaching peak shear strains (γ_{peak}) from 25% to 150% with increments of 25%. Figure 2c depicts the shear force versus shear strain curves obtained for one of the isolators for 50%, 100%, and 150% peak shear strains. Based on the isolator tests, the effective stiffness (k_{eff}) and effective damping ratio (ξ_{eff}) are calculated (ASCE 2010) as:

$$k_{eff} = \frac{|F^+| + |F^-|}{|\Delta^+| + |\Delta^-|}; \quad \xi_{eff} = \frac{2}{\pi} \frac{E_{loop}}{k_{eff}(|\Delta^+| + |\Delta^-|)^2} \tag{1a,b}$$

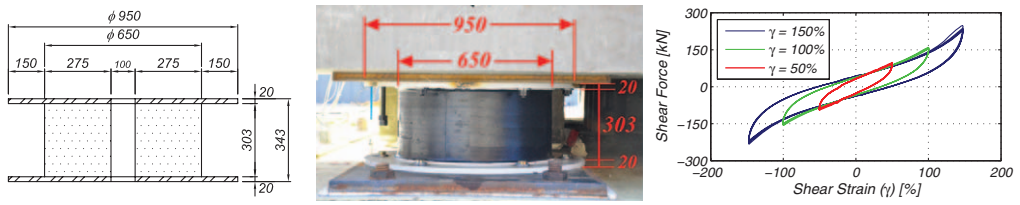

(a) (b) (c)

Figure 2. Seismic isolator bearing: (a) Schematic view; (b) Isolator installed in the NE corner; (c) hysteretic curves of quality control tests. (Dimensions in mm.)

Table 1. Effective properties (k_{eff} and ξ_{eff}) of the HDRBs obtained from component tests

		Peak shear strain γ_{peak} [%]					
Bearing	Property	25	50	75	100	125	150
1	k_{eff} [kN/m]	1,313	918	793	742	743	752
	ξ_{eff} [%]	19.0	17.1	15.2	13.8	12.3	10.6
2	k_{eff} [kN/m]	1,442	1,003	845	764	727	701
	ξ_{eff} [%]	18.5	16.7	15.1	14.0	12.9	11.3
3	k_{eff} [kN/m]	1,422	971	832	766	758	756
	ξ_{eff} [%]	19.3	17.1	15.1	13.7	12.2	10.5
4	k_{eff} [kN/m]	1,430	992	849	772	748	749
	ξ_{eff} [%]	19.2	16.9	14.9	13.3	12.1	10.3
Sum	$k_{eff\ total}$ [kN/m]	5,607	3,884	3,319	3,044	2,976	2,958

where Δ^+, Δ^- are the maximum (positive) and minimum (negative) horizontal displacements of the isolator during a cycle, F^+, F^- are the maximum (positive) and minimum (negative) forces at Δ^+, Δ^-, respectively, and E_{loop} is the energy dissipated in one hysteresis loop over displacement range from Δ^+ to Δ^-. Table 1 shows the values of k_{eff} and ξ_{eff} obtained from the bearing tests. For each shear strain level, the values obtained for different bearings are very close to each other. The effective stiffness of the isolators was around 1400 kN/m for $\gamma_{peak} = 25\%$, and it was gradually reduced until reaching an almost constant value of approximately 750 kN/m for $\gamma_{peak} \geq 100\%$. ξ_{eff} decreases gradually as soon as γ_{peak} increases, from a value near to 19% for $\gamma_{peak} = 25\%$ until a value around 10.5% for $\gamma_{peak} = 150\%$. Figure 3 depicts the relationship between the total effective stiffness (sum of the effective stiffness of the four isolators) and the bearing shear strain. A fourth-order polynomial curve was fitted to the data, whose equation and coefficient of determination (R^2) are shown in the figure.

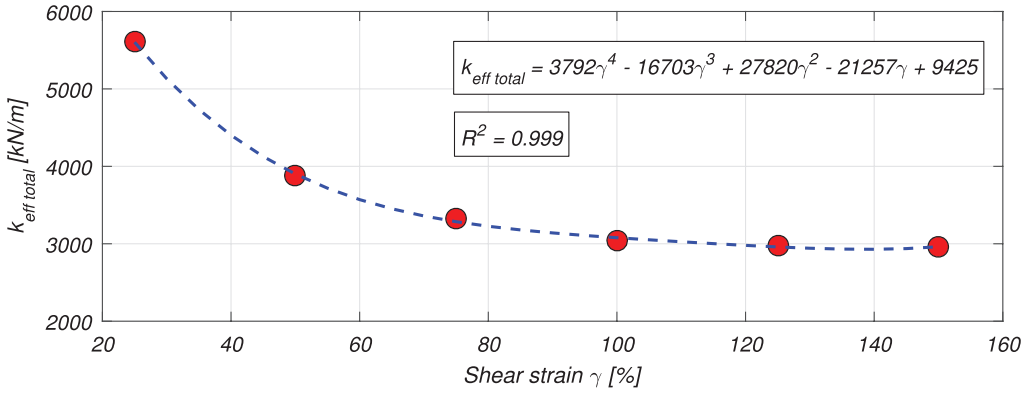

Figure 3. Total effective stiffness (sum) versus shear strain of the isolation system.

INSTRUMENTATION

A dense instrumentation array including accelerometers, displacement transducers (linear and string potentiometers) and strain gauges was installed to record different structural responses. Four triaxial accelerometers were installed on each floor close to the corners of the slab (see Figure 1b). In addition, two triaxial accelerometers were placed on the north-east and south-west corners of the shake table platen. These accelerometers were force-balance Episensor with a full-scale of ± 4 g, a frequency bandwidth DC-200 Hz, and a wide dynamic range of 155 dB. The data acquisition system used for these accelerometers (DAQ1) was a Quanterra Q330 data loggers from Kinemetrics, Inc. and sampled data at 200 Hz. Displacement transducers and strain gauges were installed to monitor different structural components (Figure 4); they were connected to an independent DAQ that sampled data at 240 Hz and comprised eight distributed National Instruments PXI chassis (DAQ2). DAQ1 and DAQ2 were synchronized in time by employing the cross-correlation function between two collocated accelerometers from both DAQs at the south-east corner of the first floor of the building. Acceleration measurements were filtered

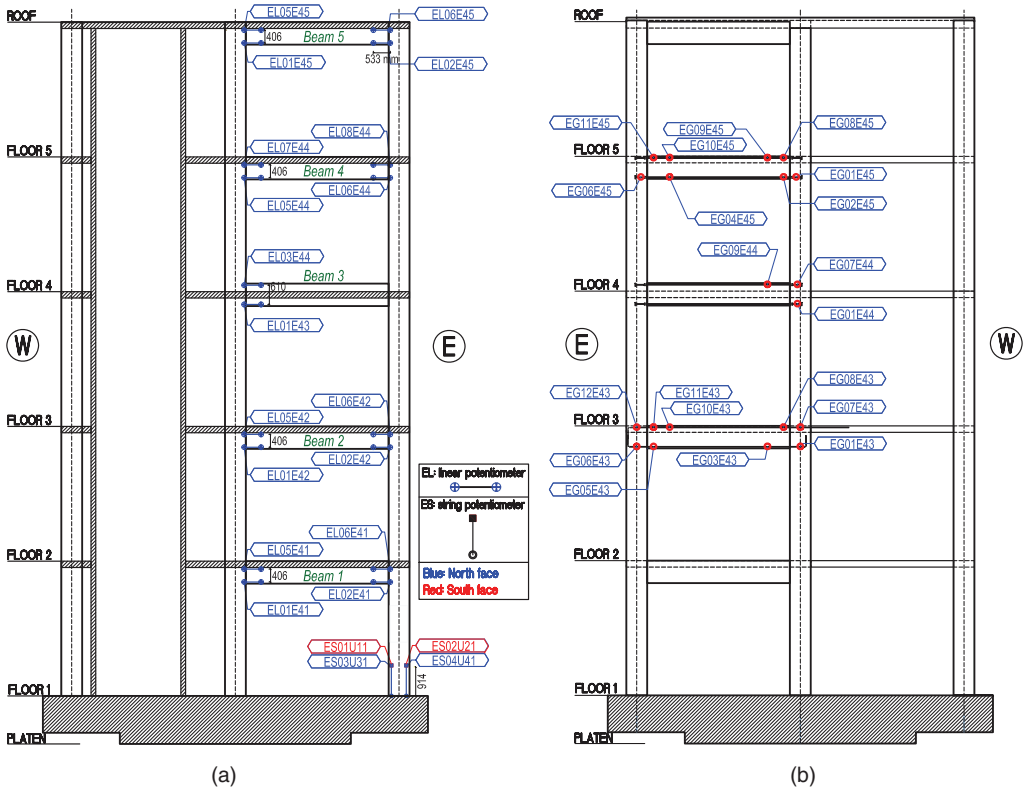

Figure 4. Instrumentation of local-level measurements: (a) Displacement transducers at beam- and column-ends; (b) strain gauges mounted on reinforcing bars of the north face of the building. (Dimensions: mm)

using a band-pass infinite impulse response (IIR) Butterworth filter of order 4 with cut-off frequencies at 0.04 and 25.0 Hz, while displacement and strain measurements were filtered using a low-pass IIR Butterworth filter of order 4 with cut-off frequency at 10.0 Hz.

SEISMIC TEST PROTOCOL

A set of seismic tests was applied to the BI building on its longitudinal direction (east-west direction) in order to progressively increase the seismic demand on the structure and its NCSs. Two serviceability-level spectrally-matched motions using the records at Canoga Park and LA City Terrace (both from the 1994 $M_s = 6.7$ Northridge earthquake) as seed motions and four actual motions, San Pedro from the 2010 $M_w = 8.8$ Maule-Chile earthquake and Ica amplitude-scaled at 50, 100, and 140% from the 2007 $M_w = 8.0$ Pisco-Peru earthquake, were applied to the building (www.strongmotioncenter.org). The input motions, peak input acceleration (PIA) and peak input displacement (PID) measured on the shake table platen, and the nomenclature used in this paper for the different seismic tests are shown in Table 2. Figure 5a shows the acceleration time-histories of the seismic input motions (measured on the shake table), while Figure 5b and Figure 5c show the corresponding displacement and pseudo-acceleration elastic response spectra (RS) for a damping ratio of 12% (value used in the design of the BI building for the design earthquake), respectively.

MEASURED AND OBSERVED RESPONSES

GLOBAL-LEVEL RESPONSE OF THE STRUCTURE

Peak floor accelerations (PFA) and peak interstory drift ratios (PIDR) along the height of the building are depicted in Figure 6. Interstory drifts were calculated with the average of the four displacements time histories obtained by double integrating the filtered acceleration time histories at the four corners of each floor of the building. PIDR in the longitudinal direction of the building (direction of shaking) were lower than 0.4% during all seismic tests and a maximum value of 0.35% (interstory drift of 14.95 mm) was reached during BI7-ICA140 (Figure 6a), despite the PID ranged between 47.6 mm (BI5-ICA50) and 129.2 mm (BI7-ICA140). The displacements imposed by the shake table were mainly absorbed by shear deformation of the isolation system (e.g., during test BI7-ICA140 the lateral deformation of the isolation system was 318 mm), confirming the effectiveness of the isolators to reduce the PIDR by concentrating the lateral deformation in the isolation layer. The effect of

Table 2. Description and nomenclature of seismic tests applied to the BI-BNCS building

Date of test	Motion	Name	PIA (g)	PID (mm)
16 April 2012	Canoga Park - 1994 Northridge EQ	BI1-CNP100	0.21	84.2
	LA City Terrace - 1994 Northridge EQ	BI2-LAC100	0.22	89.3
17 April 2012	LA City Terrace - 1994 Northridge EQ	BI3-LAC100	0.25	89.5
	San Pedro - 2010 Maule (Chile) EQ	BI4-SP100	0.52	82.7
26 April 2012	ICA 50% - 2007 Pisco (Peru) EQ	BI5-ICA50	0.17	47.6
27 April 2012	ICA 100% - 2007 Pisco (Peru) EQ	BI6-ICA100	0.32	94.6
	ICA 140% - 2007 Pisco (Peru) EQ	BI7-ICA140	0.50	129.2

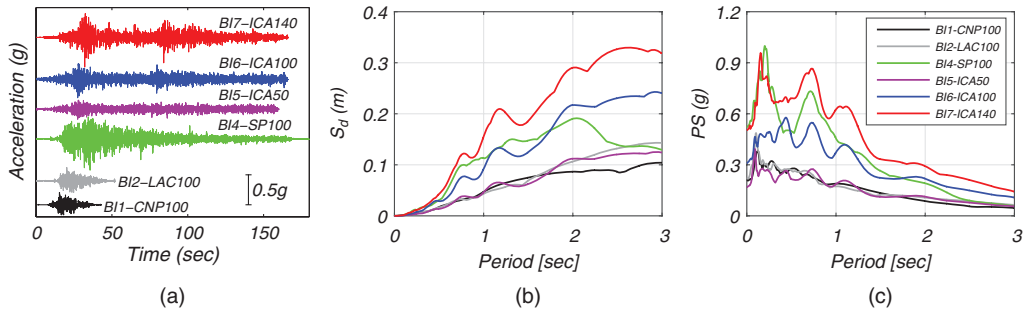

Figure 5. Input ground motions achieved on the shake table: (a) Acceleration time-histories; (b) elastic displacement response spectra ($\xi = 12\%$); (c) pseudo-acceleration response spectra ($\xi = 12\%$).

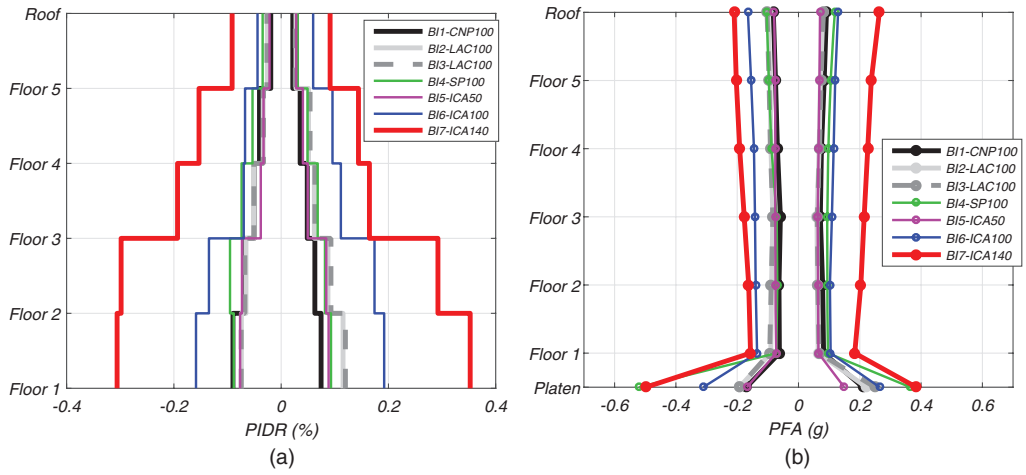

Figure 6. Global-level responses of the building: (a) Peak inter-story drift ratio (PIDR); (b) peak floor acceleration (PFA).

the isolation system in reducing the PFA compared to the PIA (at the shake table platen) is clearly observed in Figure 6b. The peak acceleration above the isolation system is about 50% of the PIA and almost no amplification is observed in the superstructure (above the isolation system) itself, which means that the dynamic amplification due to the vibration of the superstructure is very low. These low global-level responses suggest that the superstructure responded in the linear-elastic range and the isolators experienced nonlinear response during all the seismic tests.

Table 3 reports some key parameters related to the global response of the structure, including: (1) the peak roof drift ratio (PRDR) (computed as the ratio between the relative displacement between the roof and floor 1 and the height of the building); (2) the peak total

Table 3. Peak global-level responses

Test	Peak roof drift ratio *PRDR* [%]	Peak normalized base shear V_{base}/W [%]		Peak normalized base overturning moment $M_{base}/(W \times H)$ [%]
		Top of foundation	Shake table platen	
BI1-CNP100	0.05	6.86	7.05	4.48
BI2-LAC100	0.07	7.96	7.87	4.95
BI3-LAC100	0.07	8.15	7.93	5.13
BI4-SP100	0.07	8.79	9.02	5.46
BI5-ICA50	0.06	7.01	7.37	4.24
BI6-ICA100	0.12	13.39	13.79	8.34
BI7-ICA140	0.21	19.92	19.89	12.49

base shear at the top of the foundation and at the shake table platen normalized by the total weight (4,420 kN and 6,290 kN, respectively); and (3) the peak total base overturning moment normalized by the product of the total weight excluding the foundation (4,420 kN) and the roof height (21.34 m). The total base shear (V_{base}) and total base overturning moment (M_{base}) are computed as

$$V_{base}(t) = \begin{cases} \sum_{i=2}^{6} -m_i a_i(t) & \text{at top of foundation} \\ \sum_{i=1}^{6} -m_i a_i(t) & \text{at shake table platen} \end{cases} \tag{2}$$

$$M_{base}(t) = \sum_{i=2}^{6} -m_i\, h_i\, a_i(t) \tag{3}$$

where a_i is the averaged absolute floor acceleration at the i^{th} floor in the east-west direction, m_i denotes the tributary mass of the i^{th} floor, and h_i is the height of floor i measured from the top of the foundation.

The low values of the global response parameters (i.e., PIDR, PFA, PRDR, normalized base shear and base overturning moment) are an indicator of the low seismic demands experienced by the structural components during the tests. In fact, a visual inspection conducted after the last seismic test (BI7-ICA140) confirmed that the superstructure responded almost linear-elastically. Also, note that ratio $M_{base}/(V_{base} \times H)$ for the peak values is practically constant for all input motions (≈63%) and coincides with the position of center of mass of the superstructure. This suggests that the superstructure experienced a rigid-body motion response during the tests.

LOCAL-LEVEL RESPONSE OF THE STRUCTURE

Axial and flexural deformations of beam and column ends were measured using pairs of linear and string potentiometers, respectively. They were installed at the elements where the largest demands were expected (see Figure 4a). For the beams, the linear potentiometers measured the relative displacement between two points located at the beam-end, while

for the columns, the string potentiometers measured the relative displacement between a point at the column-end and the top of the foundation. The rotation and the average axial strain (over sensor length) of the beam and column ends are obtained, respectively, as:

$$\theta = \arctan\left(\frac{\delta_i - \delta_j}{h}\right) \quad [rad]; \quad \varepsilon_{ele} = \left(\frac{\delta_i + \delta_j}{2l_{ds}}\right) \tag{4a,b}$$

where δ_i, δ_j = displacement sensor (linear potentiometer for beams and string potentiometer for columns) measurements, i = bottom sensor for beams and left sensor for columns, j = top sensor for beams and right sensor for columns, h = distance between the two displacement sensors, and l_{ds} = length of the displacement sensor. Figure 7 shows the peak responses of the instrumented beam-ends of the building, that is, ends of beams located at the north face of the building (see Figure 4a). From tests BI1-CNP100 to BI6-ICA100, the rotations at both beam ends (west and east) are lower than 0.0003 rad, while during test BI7-ICA140 peak beam-end rotations reached a maximum value of 0.0021 rad at the east end of the third-floor beam. For average axial strains, a similar pattern is observed, with maximum peak values at the third floor of the building and low deformation levels. For the columns, Figure 8 depicts the peak responses at the base of south-east and north-east columns (see Figure 4a). As in the case of

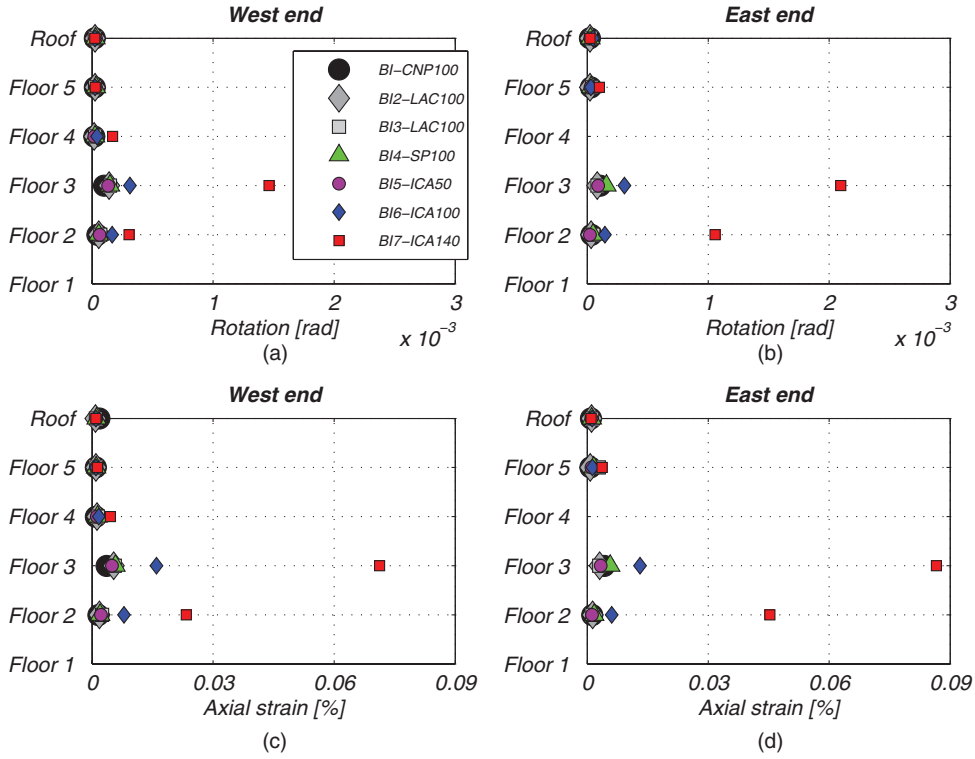

Figure 7. Beam-end peak section responses: (a) West-end rotation; (b) east-end rotation; (c) west-end average axial strain; (d) east-end average axial strain.

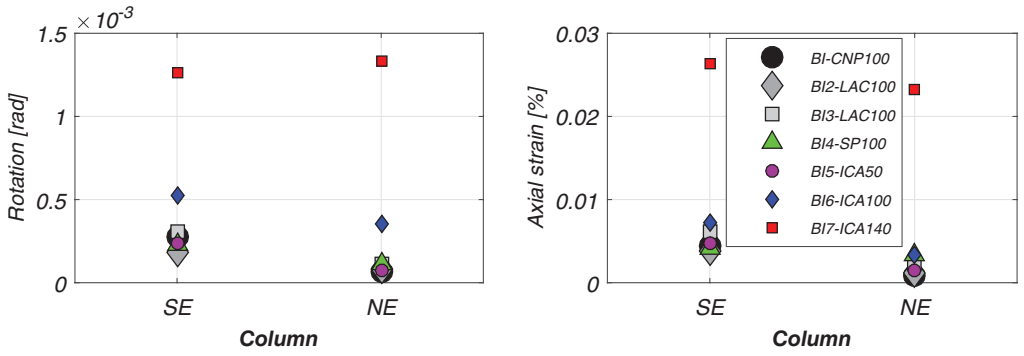

Figure 8. Column-end peak section responses: (a) Rotation; (b) average axial strain.

the instrumented beams, very low peak responses are observed for the columns, with rotations lower than 0.0015 and average axial strains lower than 0.03%. The low peak responses of all the instrumented end-elements confirm the linear-elastic response of the superstructure during the seismic tests with the building isolated at its base.

Longitudinal reinforcing bars of the beams on the north frame of the building were instrumented at different locations with strain gauges. Figure 4b shows the locations and name of the strain gauges that worked properly during all the seismic tests while the building was isolated at its base. The peak strain values of these sensors are presented in Table 4. During all the seismic tests the maximum peak strain was reached at the sensor located in the east end of the third-floor beam (EG05E43), that is, at the same location at which the maximum rotation and average axial strain of the beams were obtained. Beams on second and third floors were longitudinally reinforced with high-strength grade 100 steel (nominal yield strength $f_y = 690$ MPa) and beam on other floors with grade 60 steel (nominal yield strength $f_y = 414$ MPa). From the strain gauge values, one can conclude that none of the instrumented reinforcing bars reaches the yielding strain (>0.0019) during the seismic tests.

ISOLATION SYSTEM RESPONSE

Figure 9 shows the peak shear strain, which is computed as the ratio between the relative displacement between the top and the bottom of each isolator in the shaking direction and its total rubber height (204 mm). The peak shear strain varied from 44.5% for test BI1-CNP100 to 156% for test BI7-ICA140, and insignificant variability is observed between different isolators for all seismic tests. It is noted that the shear deformation of the isolators in the transverse direction of the building was negligible.

Figure 10 shows the hysteretic behavior of the isolation system, which is described by the total base shear (V_{base}) computed at the shake table platen (see Equation 2) normalized by the total weight of the building including the foundation (W) versus the shear strain (γ) of the isolators. The response of the isolation system is nonlinear for all the seismic tests and significant energy is dissipated due to the hysteretic behavior of the isolation system (Figure 10). During the first four seismic tests (BI-CNP100 to BI4-SP100) the shear strain of the isolation system was lower than 70%. A hardening effect is evidenced for $\gamma > 100\%$

Table 4. Peak strains recorded on the longitudinal reinforcing bars of beams

Strain gauge	Test						
	BI1-CNP100	BI2-LAC100	BI3-LAC100	BI4-SP100	BI5-ICA50	BI6-ICA100	BI6-ICA140
EG11E45	0.00004	0.00005	0.00004	0.00006	0.00005	0.00006	0.00010
EG10E45	0.00004	0.00004	0.00003	0.00004	0.00004	0.00004	0.00005
EG09E45	0.00003	0.00003	0.00004	0.00005	0.00004	0.00004	0.00007
EG08E45	0.00004	0.00003	0.00004	0.00004	0.00004	0.00005	0.00007
EG06E45	0.00004	0.00005	0.00004	0.00004	0.00008	0.00005	0.00006
EG04E45	0.00005	0.00005	0.00004	0.00005	0.00004	0.00007	0.00012
EG02E45	0.00007	0.00007	0.00005	0.00005	0.00005	0.00011	0.00011
EG01E45	0.00004	0.00004	0.00005	0.00004	0.00004	0.00006	0.00009
EG09E44	0.00006	0.00005	0.00005	0.00007	0.00005	0.00009	0.00016
EG07E44	0.00005	0.00003	0.00005	0.00006	0.00005	0.00006	0.00031
EG01E44	0.00005	0.00006	0.00007	0.00007	0.00006	0.00014	0.00032
EG12E43	0.00003	0.00003	0.00003	0.00003	0.00003	0.00004	0.00008
EG11E43	0.00008	0.00011	0.00011	0.00011	0.00009	0.00032	0.00080
EG10E43	0.00010	0.00012	0.00013	0.00009	0.00010	0.00081	0.00046
EG08E43	0.00008	0.00006	0.00004	0.00010	0.00007	0.00011	0.00071
EG07E43	0.00002	0.00002	0.00002	0.00003	0.00002	–	0.00008
EG06E43	0.00003	0.00002	0.00002	0.00002	0.00003	0.00003	0.00007
EG05E43	0.00047	0.00041	0.00043	0.00065	0.00044	0.00088	0.00180
EG03E43	0.00007	0.00007	0.00009	0.00007	0.00010	0.00009	0.00008
EG01E43	0.00001	0.00002	0.00002	0.00002	0.00002	0.00004	0.00007
Max	**0.00047**	**0.00041**	**0.00043**	**0.00065**	**0.00044**	**0.00088**	**0.00180**

during the last test BI7-ICA140 (Figure 10b), which is consistent with the hysteretic curves obtained from the component tests (see Figure 2c).

SYSTEM IDENTIFICATION

In this section, the dynamic characteristics of the building will be investigated by analyzing the time-variant modal properties of the building during the seismic tests. To this end, the DSI method is used with input-output acceleration data recorded in the building to estimate the instantaneous modal properties of the building by employing a short-time windowing approach.

METHOD

A discrete-time linear time-invariant (LTI) state-space (SS) model can be written as (Van Overschee and De Moor 1996):

$$\mathbf{x}_{k+1} = \mathbf{A_d}\mathbf{x}_k + \mathbf{B_d}\mathbf{u}_k + \mathbf{w}_k \tag{5a}$$

$$\mathbf{y}_k = \mathbf{C_d}\mathbf{x}_k + \mathbf{D_d}\mathbf{u}_k + \mathbf{v}_k \tag{5b}$$

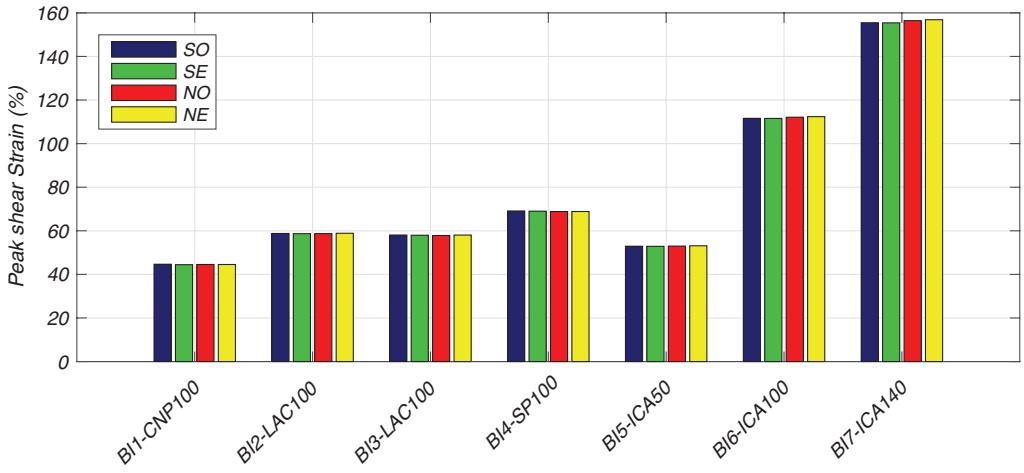

Figure 9. Peak shear strain in the seismic isolation bearings.

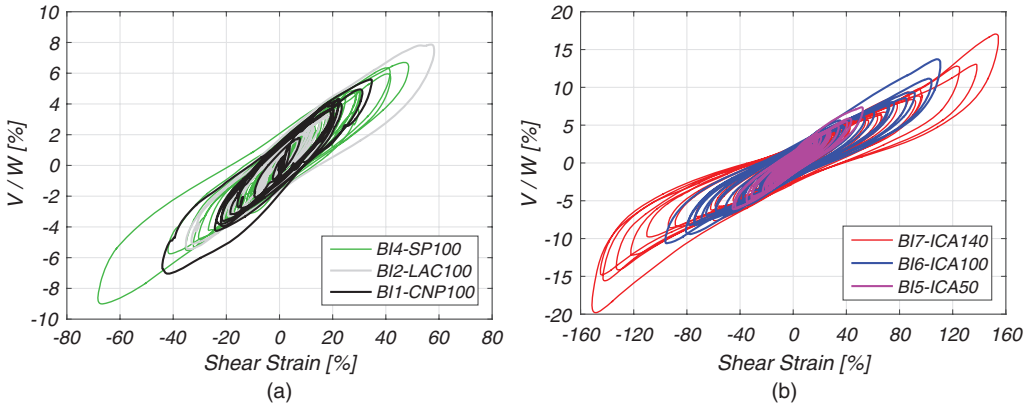

Figure 10. Normalized total base shear (at the shake table platen) versus shear strain in the seismic isolation system: (a) Tests BI1-CNP100, BI2-CNP100 and BI4-SP100; (b) Tests BI5-ICA50, BI6-ICA100, BI7-ICA140.

with:

$$E\left[\begin{pmatrix}\mathbf{w}_p\\ \mathbf{v}_p\end{pmatrix}\begin{pmatrix}\mathbf{w}_q^T & \mathbf{v}_q^T\end{pmatrix}\right]=\begin{pmatrix}\mathbf{Q} & \mathbf{S}\\ \mathbf{S}^T & \mathbf{R}\end{pmatrix}\delta_{pq}\geq 0, \tag{6}$$

where $\mathbf{x}_k \in \mathbb{R}^n$ = state vector, $\mathbf{y}_k \in \mathbb{R}^l$ = measured output vector (i.e., l = number of outputs), $\mathbf{u}_k \in \mathbb{R}^m$ = measured input vector (i.e., m = number of inputs), $\mathbf{A_d} \in \mathbb{R}^{n\times n}$ = state matrix, $\mathbf{B_d} \in \mathbb{R}^{n\times m}$ = input matrix, $\mathbf{C_d} \in \mathbb{R}^{l\times n}$ = output matrix, $\mathbf{D_d} \in \mathbb{R}^{l\times m}$ = direct feed-through matrix, $\mathbf{w}_k \in \mathbb{R}^n$ and $\mathbf{v}_k \in \mathbb{R}^l$ = process and measurement noise, respectively, $\mathbf{Q} \in \mathbb{R}^{n\times n}$,

$\mathbf{S} \in \mathbb{R}^{n\times l}$ y $\mathbf{R} \in \mathbb{R}^{l\times l}$ are the covariance matrices associated to $\mathbf{w}_k$ and $\mathbf{v}_k$, δ_{pq} denotes the Kronecker delta (i.e., $\delta_{pq} = 0$ if $p \neq q$ and $\delta_{pq} = 1$ if $p = q$), and k denotes the discrete time instant.

The objective of a system identification method is to find the order (n) and the matrices of the system ($\mathbf{A_d}, \mathbf{B_d}, \mathbf{C_d}, \mathbf{D_d}, \mathbf{Q}, \mathbf{R}$ and $\mathbf{S}$) given s measurement samples of the input ($\mathbf{u}_0, \mathbf{u}_1, \ldots, \mathbf{u}_{s-1}$) and output ($\mathbf{y}_0, \mathbf{y}_1, \ldots, \mathbf{y}_{s-1}$) data. Using the relationship between the discrete and continuous state matrices, the modal properties of the system can be obtained by:

$$f_r = \frac{\sqrt{\lambda_r \lambda_r^*}}{2\pi} \qquad r = 1,\ldots,n/2 \tag{7}$$

$$\xi_r = \frac{-\mathrm{Re}(\lambda_r)}{|\lambda_r|} \qquad r = 1,\ldots,n/2 \tag{8}$$

$$\mathbf{\Phi} = \mathbf{C_d}\mathbf{\Psi} = [\boldsymbol{\phi}_1,\ldots,\boldsymbol{\phi}_{n/2}] \tag{9}$$

where f_r, ξ_r and $\boldsymbol{\phi}_r$ are the modal frequencies, modal damping ratios, and mode shapes, respectively; λ_r = eigenvalues of the continuous-time state matrix $\mathbf{A}_c$ (with $\mathbf{A_d} = e^{\mathbf{A}_c \Delta t}$ and Δt = sampling time), $\mathbf{\Psi}$ = eigenvectors of $\mathbf{A_d}$, and superscript * and $|\cdot|$ denote complex conjugate and magnitude, respectively.

The DSI method is employed here to identify the modal properties of the BI-BNCS building. First, input and output Hankel matrices are constructed using the recorded data. As an example, Equation 10 shows the input Hankel matrix of the system. In this equation, i = number of block rows, j = number of columns (usually $j = s - 2i + 1$), and the subscripts p and f denote past and future.

$$\mathbf{U}_{0|2i-1} = \left(\begin{array}{ccccc} \mathbf{u}_0 & \mathbf{u}_1 & \mathbf{u}_2 & \cdots & \mathbf{u}_{j-1} \\ \mathbf{u}_1 & \mathbf{u}_2 & \mathbf{u}_3 & \cdots & \mathbf{u}_j \\ \vdots & \vdots & \vdots & \cdots & \vdots \\ \mathbf{u}_{i-1} & \mathbf{u}_i & \mathbf{u}_{i+1} & \cdots & \mathbf{u}_{i+j-2} \\ \hline \mathbf{u}_i & \mathbf{u}_{i+1} & \mathbf{u}_{i+2} & \cdots & \mathbf{u}_{i+j-1} \\ \mathbf{u}_{i+1} & \mathbf{u}_{i+1} & \mathbf{u}_{i+3} & \cdots & \mathbf{u}_{i+j} \\ \vdots & \vdots & \vdots & \vdots & \vdots \\ \mathbf{u}_{2i-1} & \mathbf{u}_{2i} & \mathbf{u}_{2i+1} & \cdots & \mathbf{u}_{2i+j-2} \end{array}\right) = \left(\frac{\mathbf{U}_{0|i-1}}{\mathbf{U}_{i|2i-1}}\right) = \left(\frac{\mathbf{U}_\mathrm{p}}{\mathbf{U}_\mathrm{f}}\right) \tag{10}$$

The DSI method employs oblique projections of the row spaces of certain Hankel matrices into the row spaces of other Hankel matrices. Then, the order of the model (n), the observability matrices ($\mathbf{\Gamma}_i$ and $\mathbf{\Gamma}_{i-1}$) and state sequences ($\tilde{\mathbf{X}}_i$ and $\tilde{\mathbf{X}}_{i+1}$) are determined using singular value decomposition. Finally, the model matrices ($\mathbf{A_d}, \mathbf{B_d}, \mathbf{C_d}$ and $\mathbf{D_d}$) are obtained by solving a least squares problem. Figure 11 shows the schematic overview of the DSI method (Van Overschee and De Moor 1996). In this paper, the weighting matrices ($\boldsymbol{W}_1$ and $\boldsymbol{W}_2$) are chosen according to the N4SID algorithm (Numerical algorithms for Subspace State Space System Identification).

1. Define Hankel matrices:

$$\mathbf{U}_{0|2i-1} = \begin{pmatrix} \mathbf{U}_{0|i-1} \\ \mathbf{U}_{i|2i-1} \end{pmatrix} = \begin{pmatrix} \mathbf{U}_p \\ \mathbf{U}_f \end{pmatrix} \quad ; \quad \mathbf{Y}_{0|2i-1} = \begin{pmatrix} \mathbf{Y}_{0|i-1} \\ \mathbf{Y}_{i|2i-1} \end{pmatrix} = \begin{pmatrix} \mathbf{Y}_p \\ \mathbf{Y}_f \end{pmatrix}$$

2. Compute oblique projections:

$$\mathbf{O}_i = \mathbf{Y}_f \,/_{\mathbf{U}_f} \begin{pmatrix} \mathbf{U}_p \\ \mathbf{Y}_p \end{pmatrix} \quad ; \quad \mathbf{O}_{i+1} = \mathbf{Y}_f^- \,/_{\mathbf{U}_f^-} \begin{pmatrix} \mathbf{U}_p^+ \\ \mathbf{Y}_p^+ \end{pmatrix}$$

3. Determine order of the system using singular value decomposition:

$$\mathbf{W}_1 \mathbf{O}_i \mathbf{W}_2 = \begin{pmatrix} \mathbf{U}_1 & \mathbf{U}_2 \end{pmatrix} \begin{pmatrix} \mathbf{S}_1 & \mathbf{0} \\ \mathbf{0} & \mathbf{0} \end{pmatrix} \begin{pmatrix} \mathbf{V}_1^T \\ \mathbf{V}_2^T \end{pmatrix} = \mathbf{U}_1 \mathbf{S}_1 \mathbf{V}_1^T$$

$\boldsymbol{W}_1, \boldsymbol{W}_2$: weighting matrices

4. Compute the extended observability matrices $\boldsymbol{\Gamma}_i$ and $\boldsymbol{\Gamma}_{i-1}$:

$$\boldsymbol{\Gamma}_i = \mathbf{W}_1^{-1} \mathbf{U}_1 \mathbf{S}_1^{1/2}$$

$\boldsymbol{\Gamma}_{i-1}$ is defined by removing the last l rows of $\boldsymbol{\Gamma}_i$

5. Determine the state sequences $\tilde{\mathbf{X}}_i$ and $\tilde{\mathbf{X}}_{i+1}$:

$$\tilde{\mathbf{X}}_i = \boldsymbol{\Gamma}_i^{\dagger} \mathbf{O}_i \quad ; \quad \tilde{\mathbf{X}}_{i+1} = \boldsymbol{\Gamma}_{i-1}^{\dagger} \mathbf{O}_{i+1}$$

where $\bullet^{\dagger}$ denotes the Moore-Penrose pseudo-inverse of the matrix $\bullet$

6. Solve the set of linear equations for $\mathbf{A}_\mathbf{d}, \mathbf{B}_\mathbf{d}, \mathbf{C}_\mathbf{d}$ and $\mathbf{D}_d$ using least-squares:

$$\begin{pmatrix} \tilde{\mathbf{X}}_{i+1} \\ \mathbf{Y}_{i|i} \end{pmatrix} = \begin{pmatrix} \mathbf{A}_\mathbf{d} & \mathbf{B}_\mathbf{d} \\ \mathbf{C}_\mathbf{d} & \mathbf{D}_\mathbf{d} \end{pmatrix} \begin{pmatrix} \tilde{\mathbf{X}}_i \\ \mathbf{U}_{i|i} \end{pmatrix} + \begin{pmatrix} \boldsymbol{\rho}_w \\ \boldsymbol{\rho}_v \end{pmatrix}$$

7. Compute eigenvalues μ and eigenvectors ($\boldsymbol{\Psi}$) of the state matrix $\mathbf{A}_\mathbf{d}$.

8. Determine modal properties of the system:

$$f_r = \frac{\sqrt{\lambda_r \lambda_r^*}}{2\pi}$$

$$\xi_r = \frac{-\mathrm{Re}(\lambda_r)}{|\lambda_r|}$$

$$\boldsymbol{\Phi} = \mathbf{C}_\mathbf{d} \boldsymbol{\Psi}$$

with

$$\lambda_r = \frac{\ln(\mu_r)}{\Delta t}$$

Figure 11. Schematic overview of the used system identification method (DSI) (adapted from Van Overschee and De Moor 1996).

TIME-VARIANT MODAL PARAMETERS

To track the variation of the dynamic characteristics of the building, the instantaneous modal properties are estimated using input-output recorded data split on short-time windows. The acceleration at the shake table platen is used as input data (i.e., $m = 1$) and the longitudinal acceleration responses of the south-east corner of every floor of the building are used as output data (i.e., $l = 6$; see Figure 1b). Note that only one acceleration response per floor in the longitudinal direction of the building (direction of the input motion) is used to conduct the system identification, because the differences between the longitudinal floor accelerations

recorded at the four corners of each floor are negligible. In addition, measured transverse floor accelerations are very small.

To define the length of the time windows, the following three different criteria were investigated in Gutiérrez (2016): (1) based on the energy distribution of the input by using the Arias Intensity (Arias 1970), (2) based on fixed-length windows (e.g., 2 seconds long) with and without overlapping, and (3) the minimum length window with and without overlapping. Results based on numerically simulated response data of a liner time variant (with stiffness reduction during the earthquake response) shear building model (Zhong and Chang 2016) suggested that the minimum window length approach, which is defined in Equation 11, with a 50% overlap provides the best tracking capabilities to identify the time-varying modal properties (Gutiérrez 2016).

$$s_{\min} = 2i(m + l + 1) \tag{11}$$

In the case of the BI-BNCS building, a number of block rows of the Hankel matrices equal to $i = 45$ was obtained following the procedure presented in Rainieri and Fabbrocino (2014). This approach carries out a sensitivity analysis to determine an optimal value of i such that the level of uncertainty in the estimated modal parameters is minimized. This method provides accurate and stable estimates of the modal parameters. According to Equation 11, the minimum window length is equal to $s_{\min} = 2 \times 45(1 + 6 + 1) = 720$ for the BI-BNCS building. Because the sampling frequency is 200 Hz, the minimum window length corresponds to $720/200 = 3.6\,s$. One can observe that 50% of overlapping, which is considered for the time windows, implies that the estimation of instantaneous modal parameters is intrinsically averaged and obtained every $3.6/2 = 1.8\,s$.

For each short-window data set, stabilization diagrams (which plot the identified modal parameters versus the model order; Peeters and De Roeck 2001) are used to distinguish between physical and spurious (mathematical) modes. The following stability criteria are used:

$$|f_r - f_s|/f_s \leq 2\%; \qquad |\xi_r - \xi_s|/\xi_s \leq 10\%; \qquad (1 - \mathrm{MAC}_{\phi_r,\phi_s})100 \leq 2\%, \tag{12}$$

where f_r, f_s, ξ_r, and ξ_s are the identified natural frequencies and damping ratios for models of consecutive orders, $\mathrm{MAC}_{\phi_r,\phi_s}$ is the modal assurance criterion (MAC) (Allemang and Brown 1982) of a pair of corresponding modes shapes identified for models of consecutive orders.

Based on previous studies performed on the BI-BNCS building by using ambient vibration (AV) and low-amplitude white noise test data, the system identification is focused on frequencies below 15 Hz, which is enough to identify the first four longitudinal modes of the building (Astroza 2015). Since the shake table is uniaxial (shaking direction coincided with the longitudinal direction of the building), the contribution of torsional and transverse modes to the total response of the building is insignificant and their identification is not feasible by using the recorded data during the seismic tests. This issue is discussed in more detail for the fixed-base BNCS building by Astroza et al. (2016) when low-amplitude white noise test data was used.

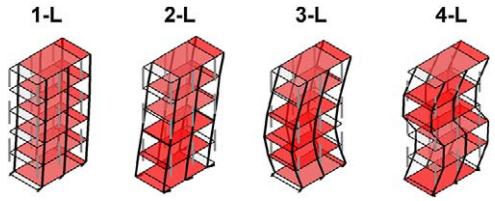

Figure 12. Identified mode shapes of the building.

The mode shapes identified with the DSI method are complex-valued and the corresponding real-valued mode shapes are computed using the method described by Imregun and Ewins (1993). Figure 12 shows the real-valued mode shapes of the building identified using the first time window of the BI1-CNP100 test. The first four longitudinal modes (1-L, 2-L, 3-L, and 4-L) of the building are properly identified. Mode 1-L involves mostly deformation of the isolation system with an almost pure rigid-body motion of the superstructure, and it is consequently referred to as isolation mode. Considerable deformation of the superstructure is observed for higher longitudinal modes (2-L, 3-L, and 4-L); however, these modes also include some deformation of the isolation system.

The effective properties of the isolation system are calculated by using the total base shear (V_{base} at the shake table platen) versus shear strain in the isolators (γ) hysteretic response of the building. The effective stiffness of the isolation layer ($k_{eff\ total}$) is computed by using Equation 1a for each hysteretic cycle. The effective damping ratio of the isolation system (ξ_{eff}) is calculated using Equation 1b. E_{loop} and the strain energy are evaluated for each V_{base} versus γ hysteretic cycle and then ξ_{eff} is computed from the total energy dissipated and total strain energy (i.e., accumulated from the beginning of each test to the current time step). To eliminate the very small amplitude response at the beginning and end of the V_{base} versus γ response, $k_{eff\ total}$ and ξ_{eff} are computed for each seismic test considering the time interval between 0.001% and 99.999% of the total Arias Intensity (Arias 1970) of the input motion.

In Figure 13, the top four plots show the identified instantaneous natural frequencies of the first four longitudinal modes of the building, the bottom plot depicts the input acceleration time-histories achieved on the shake table and the second panel (from the bottom to the top) the effective stiffness of the isolation system. In the plots of the identified natural frequencies, the frequencies identified with AV data (Astroza 2015) are shown with dashed red lines. The nonlinear response of the isolation system during all the seismic tests can be inferred from the variation of $k_{eff\ total}$ along the time.

At the beginning of each seismic test, the input motion displays low amplitudes and high values of $k_{eff\ total}$ are calculated. As soon as the amplitude of the input motion increases during the strong-motion phase, the secant stiffness of the isolation system decreases significantly, but it recovers at the end of each seismic test, reaching a value similar to the one computed at the beginning of the input motion. That is, the isolation system shows a stable (i.e., without degradation) inelastic behavior.

A very similar pattern is observed for the variation of the identified natural frequency associated with the first longitudinal mode (1-L). That is, the identified natural frequency of

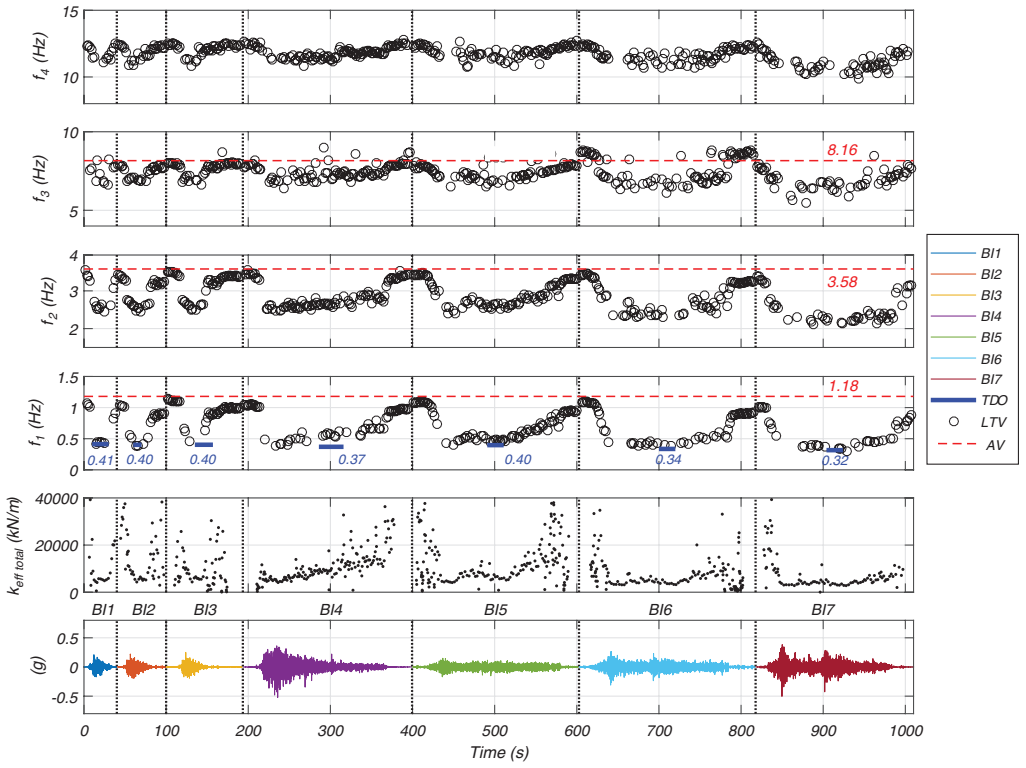

Figure 13. Temporal variation of the natural frequency of the first four longitudinal modes.

mode 1-L at the beginning and the end of each seismic test is similar to the frequency identified using AV data (i.e., 1.18 Hz). This confirms that a high lateral stiffness is provided by the HDRBs when they are subjected to low-amplitude excitations.

During the strong-motion phase, the identified natural frequency associated with mode 1-L decreases considerably until reaching minimum values into the range 0.37–0.41 Hz for tests BI1-CNP100 to BI5-ICA50 and 0.36 Hz and 0.32 Hz for tests BI6-ICA100 and BI7-ICA140, respectively. This implies that during the seismic tests, the frequency of mode 1-L experienced maximum reductions of 2.9 to 3.7 times of the frequency that is observed for low-amplitude excitations (AV). Because the mass of the building did not change during the tests, the frequency reduction is only explained due to the reduction of the lateral stiffness of the isolation system. That is, the lateral stiffness was reduced to values between 12% and 7% of the lateral stiffness at low-level excitations. This reduction agrees with the variation of $k_{eff\ total}$ that is shown in Figure 13, which changes from a maximum value of 36,000 kN/m (at low-amplitude excitations) to minimum values in the range 2,800–4,000 kN/m (during the strong-motion phase).

One can note that the lower values of the identified natural frequency obtained for mode 1-L, for each ground motion, are in good agreement with the values that were reported

by Chen et al. (2017), which are shown with blue dashes lines in Figure 13. Chen et al. (2017) estimated the predominant frequency of the BI-BNCS building by using the roof displacement during the strong-motion phase obtained from collocated accelerometers and GPS antennas (Geng et al. 2013).

The variation of the identified natural frequency of mode 1-L over time confirms that the isolation system experienced significant stiffness reduction during the seismic tests, which is almost completely recovered at the end of each seismic test. However, one can note that the identified frequency of mode 1-L at the end of a seismic test is slightly lower than that identified at the beginning of the next seismic test. This suggest that part of the stiffness degraded during a seismic test is not recovered immediately, however, it is practically completely recovered at the beginning of the next seismic test. This temporary and recoverable stiffness reduction in HDRBs is known as Mullins' effect and has been previously observed in BI structures instrumented during earthquakes (e.g., Siringoringo and Fujino 2014).

Natural frequencies identified for higher longitudinal modes (2-L, 3-L, and 4-L) exhibit similar variations during the time, decreasing during the strong-motion part of the seismic excitations. However, for these modes the relative reduction in frequency (with respect to natural frequencies identified with low-amplitude vibration data) is much lower (relatively speaking) than the reduction observed for model 1-L. For mode 2-L, the identified frequency in the strong-motion phase is about 70% of that identified with AV data, while for modes 3-L and 4-L is about 85%. Higher modes also experience reduction in their identified natural frequencies because these modes also involve deformation of the isolation system (see Figure 12), and not because of damage in the superstructure. An excellent agreement between the identified time-varying natural frequencies at the beginning and end of seismic tests and those identified from AV (Astroza 2015) is also observed for higher modes.

The identification of almost the same natural frequencies for all longitudinal modes (direction of excitation) at the beginning of the first seismic test (BI1-CNP100) and at the end of the last seismic test (BI7-ICA140) suggests that the building did not suffer reduction of stiffness during the strong motions, which means that the building did not suffer structural damage. This conclusion is in agreement with the low demands of the building, at the global and local levels, that were previously reported in this paper, and also with the visual inspections conducted after seismic test BI7-ICA140.

The top four plots of Figure 14 show the instantaneous identified equivalent viscous damping ratios for the first four longitudinal modes of the building, that is, 1-L, 2-L, 3-L, and 4-L. In these plots, the damping ratios identified with AV data by Astroza (2015) are displayed with dashed red lines. Similarly, the damping ratio of the predominant mode estimated during the strong-motion phase by using the roof displacement that was obtained by Chen et al. (2017) is depicted with blue dashed lines. The bottom and second (from bottom to top) plots show the input motion time-histories that were achieved on the shake table and the effective damping (ξ_{eff}) computed by using the hysteretic response of the isolation layer according to the procedure that was previously explained. The damping ratio identified for mode 1-L is significantly larger than those identified for higher modes, and its values during the strong-motion phase correlates properly with ξ_{eff}.

For mode 1-L, the identified damping ratio increases considerably from values around 5% during the beginning of the input motions to values as large as 12–25% during the

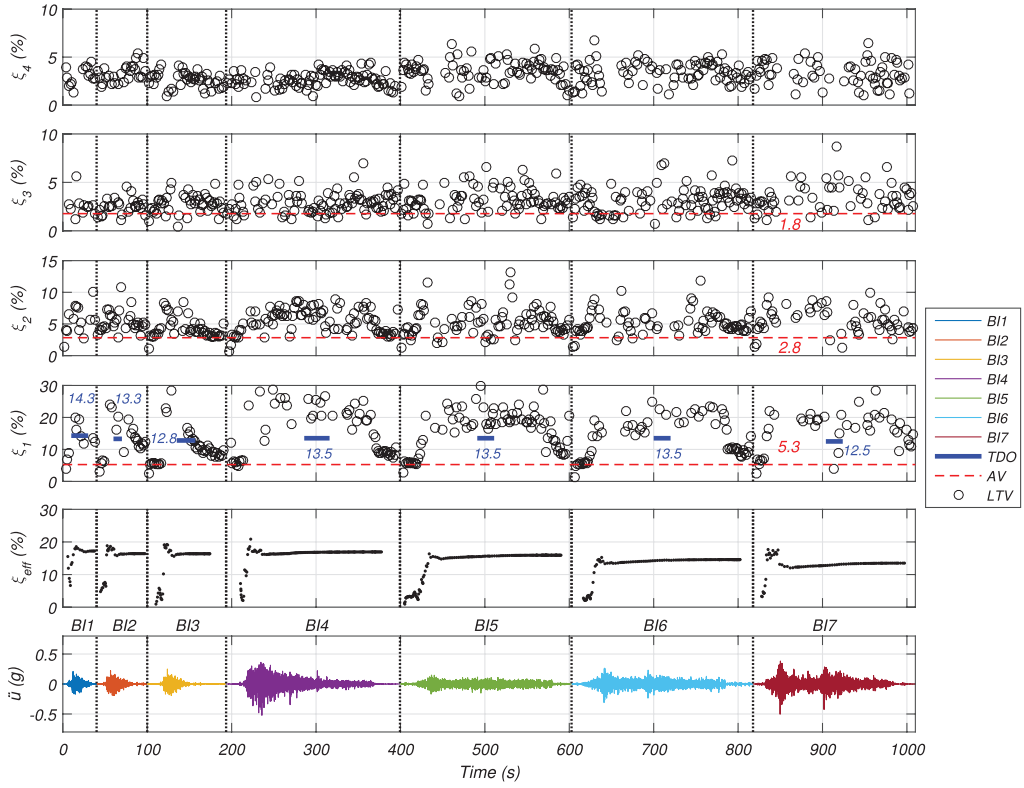

Figure 14. Temporal variation of the damping ratio for the first four longitudinal modes.

strong-motion phase, and then these values decrease again during the end of the seismic tests, reaching values around 5%. This damping ratio is in excellent agreement with the damping ratio of mode 1-L that was identified with AV data ($\xi = 5.3\%$). Mode 1-L comprises large shear deformation of the bearings (Figure 12) and is highly related to the hysteretic response of the isolation system. Because of the underlying mathematical model considered in the system identification method employed here, all the sources of energy dissipation, in particular the energy dissipated by the bearings, are identified as an equivalent viscous damping. This modeling assumption implies that the damping ratio estimates exhibit a larger scattering than those of the natural frequencies. It is noted that the damping ratios identified for mode 1-L during the strong motion phase of the seismic excitations are slightly larger than those computed from the hysteretic response of the isolation system. Furthermore, the effective damping ratios computed from the component tests (see Table 1) are lower than those estimated for mode 1-L using the seismic test data at similar level of shear strain in the isolators, suggesting that other mechanisms, additional to the isolation system, also contributed to the energy dissipation of the BI-BNCS building during the seismic tests.

Damping ratios identified for higher longitudinal modes (2-L, 3-L, and 4-L) are considerably lower than those identified for mode 1-L. For mode 2-L, the identified damping ratio

Table 5. Comparison of approximated and identified fundamental frequency of the building

Test	Peak shear strain [%]	$k^{est}_{eff\ total}$ at peak shear strain [kN/m]	f^{app}_{1-L} [Hz]	$f^{ID}_{1-L,\min}$ [Hz]
BI1-CNP100	45	4,149	0.40	0.41
BI2-LAC100	59	3,603	0.38	0.39
BI3-LAC100	58	3,626	0.38	0.42
BI4-SP100	69	3,376	0.37	0.38
BI5-ICA50	53	3,787	0.39	0.40
BI6-ICA100	112	3,015	0.35	0.36
BI7-ICA140	156	3,014	0.35	0.32

varies from 2.5% to 8.5% and for modes 3-L and 4-L between 1.0 and 5.0%. Although damping ratios of higher modes also tend to increase during the strong-motion phase of the imposed input motion, they do not vary at the same scale as that of mode 1-L.

The temporal variation of the mode shapes is also investigated by using the MAC (Allemang and Brown 1982). It is observed that the MAC values (assuming the mode shapes identified at the beginning of test BI1 as a reference) tend to slightly decrease in the strong motion part and then they recover to values close to 1.0. However, no significant reduction is observed and the MAC values remain higher than 0.95.

The minimum effective stiffness of the isolation system ($k_{eff\ total}$) can be estimated by using the equation that appears in the Figure 3 associated with the peak shear strain experienced by the bearings during each seismic test. This value can then be used to estimate the approximated frequency of the fundamental mode of the building (f^{app}_{1-L}) as follows.

$$f^{app}_{1-L} = \frac{1}{2\pi}\sqrt{\frac{k^{est}_{eff\ total} \cdot g}{W}} \tag{13}$$

Table 5 shows the values of the peak shear strain, $k^{est}_{eff\ total}$, and f^{app}_{1-L} for all the shake table tests. One can observe that f^{app}_{1-L} is in good agreement with the lowest identified instantaneous natural frequency obtained for mode 1-L ($f^{ID}_{1-L,\min}$). This suggests that the component test data allow estimating the fundamental frequency of the building for a wide range of peak shear strain with a high accuracy.

CONCLUSIONS

The experimental data collected from a series of seven shake table tests that were carried out on a full-scale, five-story base-isolated (BI) RC building, which was tested at the UC San Diego, was used to analyze its measured and observed responses and correlate them with the variation of the instantaneous modal properties of the building.

The distribution of global and local parameters associated to the structural response were analyzed, including the peak floor accelerations and peak interstory drifts, the base shear and overturning moment, the response of the isolation system, the axial and flexural deformations of beam and column ends, and measured strains of reinforcing steel bars of beams.

The benefits of the isolation system in reducing the structural demands at global and local levels were clearly observed and it was confirmed that the superstructure behaved linear elastically.

The first four longitudinal modes of the building were identified using the deterministic-stochastic subspace identification method with input-output acceleration data recorded during the seismic tests. The instantaneous (i.e., time-varying) modal properties of the building were identified by employing a short-time windowing approach and correlated with the responses observed in the building, mainly related to the isolation system. The nonlinear behavior of the isolation layer was demonstrated by tracking the changes in the identified natural frequencies and equivalent damping ratios of the building at different levels of excitation. The stiffness reduction and energy dissipation of the bearings were detected by tracking the variation of the identified instantaneous natural frequencies and damping ratios of the building, respectively. A good correlation between the variation of the effective stiffness and effective damping ratio of the isolation system with the identified instantaneous frequency and instantaneous damping ratio of the fundamental mode (isolation mode) of the building were observed. The Mullins' effect in the bearings could also be observed in the time-varying system identification results.

Natural frequencies of higher longitudinal modes also varied during the seismic tests but relatively less than that of the fundamental longitudinal mode. Damping ratios identified for higher modes did not vary at the same scale as that of the first mode and were significantly lower than those identified for the isolation mode. Instantaneous modal properties identified during the beginning and the end of each seismic test were in excellent agreement with the results obtained by using ambient vibration data. Finally, by comparing the fundamental frequencies estimated using the component test data and those identified using the seismic test data, it was concluded that they match very well, therefore, the information obtained from component-tests allows to have a very good estimate of the fundamental frequency of the building for a wide range of input intensities.

ACKNOWLEDGMENTS

The authors acknowledge the access to the "Full-Scale Structural and Nonstructural Building System Performance during Earthquakes" project database (DOI: 10.4231/D38W38349) though the NEES Project Warehouse (https://nees.org/warehouse/project/722). The authors are very grateful to Professors Tara C. Hutchinson, Joel P. Conte, and José I. Restrepo from the University of California, San Diego for making these data available. R. Astroza acknowledges the financial support from the Universidad de los Andes–Chile through the research grant *Fondo de Ayuda a la Investigación* (FAI) and from the Chilean National Commission for Scientific and Technological Research (CONICYT), FONDECYT project No. 11160009.

REFERENCES

Allemang, R. J., and Brown, D. L., 1982. A correlation coefficient for modal vector analysis, in *Proceedings, 1st International Modal Analysis Conference (IMAC I)*, 8–10 November 1982, FL.

Arias, A., 1970. A measure of earthquake intensity, in *Seismic design for nuclear power plants* (R. Hansen, ed.), MIT Press, Cambridge, MA, 438–483.

American Society of Civil Engineers (ASCE), 2010. *Minimum Design Loads for Buildings and Other Structures, ASCE/SEI 7-10*, Reston, VA.

Astroza, R., 2015. *Vibration-Based Health Monitoring and Mechanics-Based Nonlinear Finite Element Model Updating of Civil Structures*, Ph.D. dissertation, University of California, San Diego.

Astroza, R., Ebrahimian, H., Conte, J. P., Restrepo, J. I., and Hutchinson, T. C., 2016. System identification of a full-scale five-story reinforced concrete building tested on the NEES-UCSD shake table, *Structural Control and Health Monitoring* **23**, 535–559.

Celebi, M., 1996. Successful performance of a base-isolated hospital building during the 17 January 1994 Northridge earthquake, *The Structural Design of Tall Buildings* **5**, 95–109.

Chen, M. C., Pantoli, E., Wang, X., Astroza, R., Ebrahimian, H., Hutchinson, T. C., Conte, J. P., Restrepo, J. I., Marin, C., Walsh, K., Bachman, R., Hoehler, M., Englekirk, R., and Faghihi, M., 2016. Full-scale structural and nonstructural building system performance during earthquakes: Part I – Specimen description, test protocol, and structural response, *Earthquake Spectra* **32**, 737–770.

Chen, M. C., Astroza, R., Restrepo, J. I., Conte, J. P., Hutchinson, T. C., and Bock, Y., 2017. Predominant period and equivalent viscous damping ratio identification on a full-scale building shake table test, *Earthquake Engineering & Structural Dynamics* **46**, 2459–2477.

Furukawa, T., Ito, M., Izawa, K., and Noori, M., 2005. System identification of base-isolated building using seismic response data, *ASCE Journal of Engineering Mechanics* **131**, 268–275.

Furukawa, S., Sato, E., Shi, Y., Becker, T. C., and Nakashima, M., 2013. Full-scale shaking table test of a base-isolated medical facility subjected to vertical motions, *Earthquake Engineering & Structural Dynamics* **42**, 1931–1949.

Geng, J., Melgar, D., Bock, Y., Pantoli, E., and Restrepo, J. I., 2013. Recovering coseismic point ground tilts from collocated high-rate GPS and accelerometers, *Geophysical Research Letters* **40**, 5095–5100.

Gutiérrez, G., 2016. *Linear Time-Variant and Linear Time-Invariant Modal Properties of a Full-Scale Five-Story Building Tested on a Shake Table*, Civil Engineering Thesis, Universidad de los Andes, Chile.

Housner, G., Bergman, L. A., Caughey, T. K., and Chassiakos, A. G., 1997. Structural control: Past, present, and future, *ASCE Journal of Engineering Mechanics* **123**, 897–971.

Imregun, M., and Ewins, D.J., 1993. Realization of complex mode shapes, in *Proceedings, 11th International Modal Analysis Conference (IMAC XI)*, 1–4 February 1993, Kissimmee, FL.

Kasai, K., Mita, A., Kitamura, H., Matsuda, K., Morgan, T. A., and Taylor, A. W., 2013. Performance of seismic protection technologies during the 2011 Tohoku-Oki earthquake, *Earthquake Spectra* **29**, S265–S293.

Loh, C-H., Weng, J-H., Chen, C-H., and Lu, K-C., 2013. System identification of mid-story isolation building using both ambient and earthquake response data, *Structural Control and Health Monitoring* **20**, 139–155.

Moaveni, B., and Asgarieh, E., 2012. Deterministic-stochastic subspace identification method for identification of nonlinear structures as time-varying linear systems, *Mechanical Systems and Signal Processing* **31**, 40–55.

Nagarajaiah, S., and Sun, X., 2000. Response of base isolated USC hospital building in Northridge earthquake, *ASCE Journal of Structural Engineering* **126**, 1177–1186.

Ogawa, N., Ohtani, K., Katayama, T., and Shibata, H., 2001. Construction of a three-dimensional, large-scale shaking table and development of core technology, *Philosophical Transactions of the Royal Society A* **359**, 1725–1751.

Pantoli, E., Chen, M. C., Hutchinson, T. C., Astroza, R., Conte, J. P., Ebrahimian, H., Restrepo, J. I., and Wang, X., 2016a. Full-scale structural and nonstructural building system performance during earthquakes: Part II – NCS damage states, *Earthquake Spectra* **32**, 771–794.

Pantoli, E., Chen, M. C., Hutchinson, T. C., Astroza, R., Conte, J. P., Ebrahimian, H., Restrepo, J. I., and Wang, X., 2016b. Landmark dataset from the building nonstructural components and systems (BNCS) project, *Earthquake Spectra* **32**, 1239–1260.

Peeters, B., and De Roeck, G., 2001. One-year monitoring of the Z24-bridge: Environmental effects versus damage events, *Earthquake Engineering & Structural Dynamics* **30**, 149–171.

Rainieri, C., and Fabbrocino, G., 2014. Influence of model order and number of block rows on accuracy and precision of modal parameter estimates in stochastic subspace identification, *International Journal of Lifecycle Performance Engineering* **1**, 317–334.

Sato, E., Furukawa, S., Kakehi, A., and Nakashima, M., 2011. Full shaking table test for examination of safety and functionality of base-isolated medical facilities, *Earthquake Engineering & Structural Dynamics* **40**, 1435–1453.

Siringoringo, D., and Fujino, Y., 2014. Long-term seismic monitoring of base-isolated building with emphasis on serviceability assessment, *Earthquake Engineering & Structural Dynamics* **44**, 637–655.

Stewart, J., Conte, J. P., and Aiken, I., 1999. Observed behavior of seismically isolated buildings, *ASCE Journal of Structural Engineering* **125**, 955–964.

Strong Motion Center, n.d. www.strongmotioncenter.org (last accessed April 2017).

Tobita, J., Izumi, M., and Katukura, H., 1988. Identification of vibration systems and nonlinear dynamics characteristics of structures under earthquake excitations, *Proceedings, 9th World Conference on Earthquake Engineering*, 2–9 August 1988, Tokyo-Kyoto, Japan.

Van Den Einde, L., Van Den Einde, L., Restrepo, J. I., Conte, J. P., Luco, J. E., Seible, F., Filiatrault, A., Clark, A., Johnson, A., Gram, M., Kusner, D., and Thoen, B., 2004. Development of the George E. Brown Jr. Network for Earthquake Engineering Simulation (NEES) large high performance outdoor shake table at the University of California, San Diego, in *Proceedings, 13th World Conference on Earthquake Engineering*, 1–6 August 2004, Vancouver, Canada.

Van Overschee, P., and De Moor, B., 1996. *Subspace Identification for Linear Systems: Theory, Implementation, Applications*, Kluwer Academic Publishers, The Netherlands.

Zhong, K., and Chang, C. C., 2016. Recursive combined subspace identification technique for tracking dynamic characteristics of structures under earthquake excitation, *Journal of Engineering Mechanics* **142**, 04016092.

(Received 28 March 2017; accepted 4 July 2017)